Structural determinants of REMORIN nanodomain formation in anionic membranes

Anthony Legrand, Daniel G.-Cava, Marie-Dominique Jolivet, Marion Decossas, Olivier Lambert, Vincent Bayle, Yvon Jaillais, Antoine Loquet, Véronique Germain, Marie Boudsocq, et al.

Structural determinants of REMORIN nanodomain formation in anionic membranes

Anthony Legrand[1], Daniel G.-Cava[2], Marie-Dominique Jolivet[1], Marion Decossas[3],Olivier Lambert[3], Vincent Bayle[4], Yvon Jaillais[4],Antoine Loquet[3], Véronique Germain[1], Marie Boudsocq[5], Birgit Habenstein[3], Marisela Vêlez Tirado[2] and Sébastien Mongrand[1*#]

[1]Laboratoire de Biogenèse Membranaire, CNRS, University Bordeaux, (UMR 5200), Villenave d'Ornon, France; [2]Laboratorio de Biofuncionalizacion de Superficies (Biofunctional Surfaces) Instituto de Catalisis y Petroleoqufmica CSIC c/Marie Curie 2. Cantoblanco, Madrid, Spain; [3]University Bordeaux, CNRS, Bordeaux INP, CBMN, UMR 5248, IECB, Pessac, France; [4]Laboratoire Reproduction et Développement des Plantes, Université de Lyon, ENS de Lyon, UCB Lyon 1, CNRS, INRA, Lyon, France; and [5]Institute of Plant Sciences Paris-Saclay (IPS2), Université Paris-Saclay, CNRS, INRAE, Université Evry, Université Paris-Cité, Gif-sur-Yvette, France

ABSTRACT Remorins are a family of multigenic plasma membrane phosphoproteins involved in biotic and abiotic plant interaction mechanisms, partnering in molecular signaling cascades. Signaling activity of remorins depends on their phosphorylation states and subsequent clustering into nanosized membrane domains. The presence of a coiled-coil domain and a C-terminal domain is crucial to anchor remorins to negatively charged membrane domains; however, the exact role of the N-terminal intrinsically disordered domain (IDD) on protein clustering and lipid interactions is largely unknown. Here, we combine chemical biology and imaging approaches to study the partitioning of group 1 remorin into anionic model membranes mimicking the inner leaflet of the plant plasma membrane. Using reconstituted membranes containing a mix of saturated and unsaturated phosphatidylcholine, phosphatidylinositol phosphates, and sterol, we investigate the clustering of remorins to the membrane and monitor the formation of nanosized membrane domains. REM1.3 promoted membrane nanodomain organization on the exposed external leaflet of both spherical lipid vesicles and flat supported lipid bilayers. Our results reveal that REM1.3 drives a mechanism allowing lipid reorganization, leading to the formation of remorin-enriched nanodomains. Phosphorylation of the N-terminal IDD by the calcium-dependent protein kinase CPK3 influences this clustering and can lead to the formation of smaller and more disperse domains. Our work reveals the phosphate-dependent involvement of the N-terminal IDD in the remorin-membrane interaction process by driving structural rearrangements at lipid-water interfaces.

SIGNIFICANCE The plasma membrane forms a selective barrier between the inside and the outside of the cell. It is a highly organized proteo-lipidic matrix that is subdivided into membrane domains necessary to fulfill its physiological functions, particularly for signal transduction. In this work, we used a range of biophysical methods to describe how a specific set of plasma membrane lipids (i.e., lecithins, particularly phosphoinositides, and sterols) and the plant protein remorin display a complex set of interactions and create remorin-enriched nanodomains in the plane of the lipid bilayer.

INTRODUCTION

Membrane nanodomain compartmentation is a common means to organize and regulate activities at the plasma membrane (PM) (1). Failure to do so may result in critical dysfunction, as exemplified for small GTPases such as the proto-oncogene Ras (2,3) or the yeast Rho GTPases Cdc42 (4). Studying the mechanisms underlying such an organization appears crucial in order to understand how membrane compartmentation impacts biological function. In this regard, a plethora of studies were performed on various PM nanodomain systems including both lipids and proteins. For example, in animals, Ras nanodomains (5,6), ganglioside GM1 nanodomains (7,8), and caveolae (9) are prominent targets of intense biochemical and biophysical studies. Unicellular organisms such as yeasts or bacteria also organize their PMs into nanodomains (10,11). Reconstitution of membrane nanodomain systems furthers our understanding of their underlying molecular mechanism and provides a formidable platform for *in vitro* biophysical studies (12-14). These studies highlight the importance of lipid species,

#Correspondence: sebastien.mongrand@u-bordeaux.fr

Anthony Legrand and Daniel G.-Cava contributed equally to this work.

Birgit Habenstein, Marisela Vêlez Tirado, and Sebastien Mongrand contributed equally to this work.

Anthony Legrand's present address is 1) Loschmidt Laboratories, Department of Experimental Biology and RECETOX, Faculty of Science, Masaryk University, Brno, Czech Republic; 2) International Center for Clinical Research, St. Anne's University Hospital Brno, Brno, Czech Republic.

particularly cholesterol and anionic phospholipids, involved in direct protein-lipid interactions. Rho-related GTPase of plants (ROP) are Rho GTPases, which are capable of forming nanoclusters in the inner leaflet of the plant PM. Single-molecule super-resolution microscopy revealed that ROP6 is stabilized by phosphatidylserine (PS) into PM nanodomains, which are required for auxin signaling (15,16).

Another well-known protein that clusters in nanodomains of the inner leaflet of the plant PM belongs to the multigenic family of proteins called remorins (REMs) (17). REMs encompass a broad range of functions from protection against abiotic stress and host-pathogen biotic interaction to inception of symbiosis and hormone signaling response (18). REMs belong to a family of six phylogenic groups with distinct N-terminal regions (17), which can label a plethora of nanodomains of different sizes, shapes, and localizations (19). REMs are bound to the PM's inner leaflet using an unconventional mode of targeting, through a C-terminal domain called REM-C-terminal anchor (REM-CA; Fig. 1 A). The inner leaflet of the plant PM, which is facing the cytosol, is highly negatively charged due to the presence of acidic phospholipids, such as PS, as well as phosphatidylinositol phosphates (PIPs), notably phosphatidylinositol 4-phosphate (PI4P) that accumulates in the PM (15,20-23). It is worth noting that PIPs can form nanodomains on their own (24-27), and polycationic peptides induce the clustering of PIPs (28).

The potato (*Solanum tuberosum*) group 1 isoform 3 REM, further called REM1.3, was particularly studied because its REM-CA is not palmitoylated (no cysteine residue is present). Therefore, the anchoring is entirely due to protein-lipid and protein-protein interactions, without the need for any posttranslational modification, notably grafting of a lipid moiety to the REM-CA. Biophysical and mutagenesis studies of this REM-CA domain displayed a complicated interaction mechanism with the PM, based on a balance between 1) electrostatic interactions through lysines and arginines and PI4P, 2) hydrophobic effects between REM-CA inside the lipid bilayer, and 3) anchor stabilization by phytosterols (29-33). Full-length REM1.3 was shown to segregate into liquid-ordered (lo) lipid domains both *in vitro* by solid-state NMR (31) and *in vivo* using an environmentally sensitive fluorescent probe (29). Our groups further evidenced the relevant role of REM1.3's coiled-coil domain, stabilized by three hydrophobic contacts led by leucine residues leading to trimerization (Fig. 1 A). Indeed, coiled-coil-disruptive single mutations from leucines to prolines resulted in a strong defect in PM targeting (34). Finally, REMs also contain an N-terminal intrinsically disordered domain (IDD; Fig. 1 A) that can be phosphorylated (35-37). Importantly, this IDD is not involved in membrane anchoring *per se* (31) but is likely important in protein-protein interactions as described for many IDDs (38,39). For example, we showed that the IDD of group 1 REMs can be phosphorylated by a calcium-dependent protein kinase isoform 3 (CPK3), and those phosphorylations induced nanodomain rearrangement with a significant increase of the mean square displacement of EOS-REM1.3 *in vivo* and a partial loss of nanodomain stability (37).

In this article, we present an *in vitro* reconstitution of a plant REM nanodomain, in a minimal synthetic membrane mimicking the PM's inner leaflet, in order to understand the mutual role of the lipids, the coiled-coil domain, and the phosphorylation status of the IDD. We yield a pictorial view of the localization process of REM1.3 in membranes up to a single-molecule level by high-resolution imaging using confocal laser scanning, cryo-electron microscopy (cryo-EM) and tapping-mode atomic force microscopy (AFM). Partitioning of REM1.3 into this newly designed anionic model membrane of a nanodomain system addressed three biologically relevant questions: 1) what is the minimal set of partners required to make REM1.3 nanodomains, 2) what is the contribution of lipids and the REM1.3 protein in nanodomain formation, and 3) how does phosphorylation of REM1.3 modify nanodomain organization? We postulate a molecular mechanism where the nanodomain formation would be REM1.3 driven and PIP- and sitosterol-dependent. In this view, phosphorylation of REM1.3 by CPK3 would modify protein-protein interactions, disrupting nanodomain organization into smaller and more disperse domains, thus phenocopying our *in vivo* observations by single-particle tracking photoactivated localization microscopy (29).

MATERIALS AND METHODS

Material and plant growth conditions

All lipids come from Avanti, with the exception of phosphoinositide mix (PIPmix) from bovine brain (P6023, Sigma-Aldrich, St. Louis, MO, USA). Glycosyl phosphatidylinositol ceramides (GIPCs) were purified from cauliflower, as described in (40). For transient expression, *Nicotiana benthamiana* plants were cultivated in controlled conditions (16 h photoperiod, 25°C). The GFP- REM1.3 *Arabidopsis thaliana* expressing line was crossed with the *pss1-3*$^{+/-}$ mutant (21). The resulting Fl progeny was grown on sulfadiazine to select *pss1-3*$^{+/-}$ seedlings, and these plants were then self-fertilized. In F2 generation, *pss1-3*$^{-/-}$ seedlings were selected on the basis of their agravitropic phenotype (15) and analyzed by confocal microscopy. GFP-positive plants were selected, and the localization of GFP-REM1.3 marker was analyzed and quantified. F3 seeds are kept heterozygous for the *pss1-3* mutation.

Protein production and purification

REM1.3$_{86-198}$ and REM1.3 were produced and purified as described in (31). GFP-REM1.3$_{86-198\ WT}$ and GFP-REM1.3$_{86-198,EEE}$ were constructed as follows from N- to C-terminal: 6His-GFP (41)-linker (LESTSPWKKAGS)-REM1.3$^{86-198}$ (wild-type [WT] or L125E/L137E/L155E [EEE]). The corresponding DNA sequences were ordered from Eurofins Genomics (Louisville, KY, USA) and cloned in pET-24a between NdeI and XhoI. They were produced in BL21-DE3-pLys cells in lysogeny broth medium with 30 µg/mL kanamycin. At OD_{600}= 0.6, 1 mM IPTG was used to induce protein expression at 18˚C overnight. Cells were pelleted at 6,000 x g for 20 min at 4˚C, resuspended in lysis buffer (20 mM HEPES, 150 mM NaCl, 20 mM imidazole, 1 mM PMSF, and 0.02% NaN_3 [pH 7.4] with complete protease inhibitor cocktail; Roche, Basel, Switzerland), and sonicated on ice. The lysate was centrifuged at 15,557 x g for 30 min at 4˚C, and the supernatant was loaded on a HisTrap column (GE Healthcare, Chicago, IL, USA) equilibrated in 20 mM HEPES, 150 mM NaCl, 20 mM imidazole, and 0.02% NaN_3 (pH 7.4). GFP-REM1.3$_{86-198}$ was eluted with elution buffer (20 mM HEPES, 150 mM NaCl, 400 mM imidazole, and 0.02% NaN_3 [pH 7.4]) and dialyzed against 10 mM HEPES, 150 mM NaCl, and 0.02% NaN_3 (pH 7.4) at 4˚C overnight, which triggered protein aggregation (34). The turbid protein sample was centrifuged at 100,000 x g for 2h at 4˚C, the supernatant was discarded, and the pellet was resuspended in 10 mM HEPES, 10 mM NaCl, and 0.02% NaN_3 (pH 7.4). After two more rounds of centrifugation, the last supernatant was kept and contained non-aggregated pure GFP-REM1.3$_{86-198}$. Protein concentration was assessed by absorbance at 280 nm (ε_{280} = 41,400 M^{-1} cm^{-1} according to Expasy ProtParam). All proteins were stored at 4˚C.

Recombinant CPK3-GST (WT and dead D202A mutant) was produced in BL21-DE3-pLys and purified as previously reported (42).

Structure prediction

PsiPred (43) and ColabFold (44) were used to predict the structures of REM$_{86-198,\ WT}$, REM$_{86-198,\ PPP}$, and REM$_{86-198,\ EEE}$. Protein models were visualized with PyMol (The PyMOL Molecular Graphics System, v.1.2r3pre, Schrodinger, New York, NY, USA, https://pymol.org).

Giant unilamellar vesicle (GUV) formation

Lipids at 10 g/L were mixed in organic solvent with 1% (w/w) of di-oleoylrhodamine-phosphoatidylethanolamine (RhodPE). About 20 µL mixture were spread on Teflon disks, which were individually stored in small beakers. They were dried for at least 1 h under vacuum with desiccator. Using a bubbler, lipids were prehydrated under a stream of N_2-saturated H_2O for 20 min. About 5 mL 300 mM sucrose was gently layered on top of the disk (enough volume to cover it fully). From this point, care was taken not to shake the beaker to avoid breaking nascent GUVs. After an overnight incubation at 34˚C, GUVs were collected using a severed pipette tip (to avoid shearing) and stored at 4˚C until further use. GUVs were stable for 1 week.

Fluorescence microscopy on GUVs

Teflon-coated 50 µL observation chambers were coated with 5% BSA for 20 min at room temperature and then washed three times with 10 mM Tris and 150 mM NaCl (pH 7.4). Using a severed P200 pipette tip, a drop of the GUV suspension was deposited, followed by about $1.8.10^{-12}$ mol of GFP-tagged protein. A slightly elevated cover slide was installed using double-tape face. Observations were carried out through optical oil on a Zeiss LSM 880 confocal laser scanning microscopy system (Leica, Wetzlar, Germany) equipped with argon, DPSS, and He-Ne lasers and a hybrid detector. GFP was excited at 488 nm, and RhodPE was excited at 565 nm.

Plant cell live imaging

Live imaging was performed using a Zeiss LSM 880 confocal laser scanning microscopy system. GFP and YFP fluorescence were observed with an excitation wavelength of 488 nm and emission wavelengths of 490-550 nm. Subcellular localization of YFP-REM1.3$_{WT}$ and YFP-REM1.3$_{EEE}$ was observed 48 h after infiltration of 3-week-old *N. benthamiana* leaves with *Agrobacterium tumefasciens* GV3101 carrying the appropriate constructs (OD_{600nm} = 0.2). For imaging of *Arabidopsis thaliana* root seedlings, plants were grown vertically for 6 days on a half-strength MS plate in controlled conditions (16 h photoperiod, 22˚C). The PM spatial clustering index (SCI) was calculated based on images taken from epidermal cells of the elongation zone of 6-day-old root seedlings. In order to quantify, experiments were performed using identical confocal

acquisition parameters. The SCI was calculated as previously described in (29). Briefly, 10 µm lines were plotted across the samples, and the SCI was calculated by dividing the mean of the 5% highest values by the mean of 5% lowest values. Three lines were randomly plotted per cell.

Cryo-EM

Lipids were hydrated to 10 g/L with 10 mM HEPES, 150 mM NaCl, and 0.02% NaN_3 (pH 7.4), submitted to five freeze-thaw-vortex cycles (liquid N_2, 42°C water bath), mixed with GFP-REM1.3_{86-198} to final concentrations of 0.5 g/L lipids and 0.9 µM GFP-REM1.3_{86-198}, and then incubated at room temperature for 1 to 2 h. Samples were loaded on glow-discharged holey carbon-coated copper 300 mesh grids, blotted with a filter paper, and frozen in liquid ethane using an EM-GP plunge freezer (Leica). Images were acquired on a Tecnai F20 electron microscope (Thermo Fisher Scientific, Waltham, MA, USA) operated at 200 kV using an Eagle 4k_4k camera (Thermo Fisher Scientific).

AFM

Lipids were mixed in $CHCl_3$ (or $CHCl_3$/MeOH [2/1 vol/vol] for PIPmix), dried under a gentle flow of N_2, resuspended in 10 mM HEPES and 10 mM NaCl (pH 7.4) buffer to 1-2 mg/mL at 40°C, and extruded 25 times at a temperature of 40°C by passing the solution through a polycarbonate membrane of 0.05 µm pore size (Avanti Mini-Extruder). A liposome solution was incubated on a mica surface at 30°C overnight in a sealed Petri dish at high humidity, where liposomes fused together to form a homogeneous supported lipid bilayer. Such bilayers remain homogeneous for 1 to 2 h at room temperature (20°C). To make heterogeneous supported lipid bilayers, incubation was performed at room temperature.
The mica surface was thoroughly rinsed with water to remove excess liposomes. First, pure lipid bilayers were imaged. Then, REM1.3 or REM1.3_{86-198} was added in a 250:1 lipid/protein molar ratio and allowed to incubate for 30 min. The surface was then rinsed with buffer to remove unbound protein before imaging. Images were taken with an AFM from Agilent (Santa Clara, CA, USA), model 5500, in tapping mode at room temperature. The AFM tips used were specific for soft tapping and were gold coated with a spring constant of 0.28 N/m.

In vitro REM phosphorylation assay

The *in vitro* kinase assay was performed as previously described (37). Briefly, CPK3-GST (WT or D202) was incubated with 1-2 µg REM1.3 in the kinase reaction buffer (20 mM Tris HCl [pH 7.5], 10 mM $MgCl_2$, 1 mM DTT, 50 µM cold ATP, ATP [γ-33P] 2 µCi per reaction, 1 mM $CaCl_2$) for 30 min at room temperature. The reaction was stopped with Laemmli buffer. Protein samples were heated at 95°C for 3 min and separated by SDS-PAGE on 12% acrylamide gel. After migration, the gel was dried before exposure against a phosphorScreen to reveal radioactivity on a Typhoon imaging system (GE Heathcare). The gel was then rehydrated for Coomassie staining.

RESULTS

Anchoring of REM1.3 to lipid vesicles mimicking the inner leaflet of a plant PM

A first step toward reconstituting nanodomains of REM1.3 *in vitro* was to produce GUVs containing both saturated and unsaturated phosphatidylcholine (PC) (namely dipalmitoyl-PC [DPPC] and dilinoleoyl-PC [DLPC]) and 8 mol % β-sitosterol, a well-established lipid mixture to promote lipid phase separation into lo and liquid-disordered (ld) domains at room temperature (25,45). In addition, GUVs were supplemented with 16 mol % of a mix of PIPs and PS (called PIPmix, containing 50/20/15/15 mol % of PS/PI/PIP/PIP**2** (29)). These lipids are the major anionic lipids constituting the PM's inner leaflet, to which REM1.3 is expected to bind (29,31). The inside of these GUVs is made of a 300 mM sucrose, while the outer compartment is made of a 310 mOsm Tris/NaCl buffer with traces of sucrose. Such hypertonicity is necessary to ensure GUV stability. Since sucrose is a hydrosoluble, polar, and noncharged molecule and as it is mainly located inside the GUVs, while REMs will be added to the outer compartment, we assume it will not significantly impact lipid-protein interactions and subsequent lateral segregation in the membrane plane. To assess protein binding, we used a truncated GFP-tagged REM1.3, GFP- REM1.3_{86-198} (Fig. S1), lacking its N-terminal IDD so that only the minimal anchoring machinery remains (Fig. 2 A). Images were taken by confocal microscopy after the addition of GFP-REM1.3_{86-198} to the GUVs. As expected, GFP-REM1.3_{86-198} decorated 77% of the GUVs containing the PIP/PS lipid mixture (Table S1), but not those containing only PC and sitosterol, with which the GFP fluorescence signal remained in the buffer (Fig. 1 B). RhodPE labeling was nonuniform, indicating a partial phase separation (Fig. 1 B), even in the absence of protein. This is expected for a complex mixture of high- and low-

phase transition temperature PCs, i.e., DPPC and DLPC, sitosterol, and anionic lipids, i.e., palmitoyl-oleoyl-PS (POPS) and PIPs (46-48). Likewise, GFP-REM1.3$_{86-198}$ labeling of liposomes was heterogeneous, partially mimicking, although with a much broader size, what can be observed *in vivo* for REM1.3 at the PM (Fig. 3,A and D).

Coiled-coil homo-oligomerization of REM1.3 is essential for PM anchoring

We previously showed that REM1.3's coiled-coil domain was crucial for membrane targeting *in vivo* (34). Targeting was drastically hampered by mutation of its three conserved hydrophobic core residues L126, L137, and L155 to prolines. However, proline mutations induce helix bending (Fig. S2). We wished to inquire whether the disruption of the helical fold, or the lack of oligomerization, was responsible for this behavior. In order to maintain helical integrity, we mutated L126, L137, and L155 to negatively charged glutamates (REM1.3$_{EEE}$) (Figs. 1 A and S2). Confocal microscopy showed that GFP-REM1.3$_{86-198,EEE}$ could only bind to 6% of all observed GUVs *in vitro* and that most of the GFP fluorescent signal stayed in the buffer (Fig. 1 B). We further confirmed *in vivo* that full-length YFP-REM1.3$_{EEE}$ was unable to attach to the PM and stayed in the cytosol when transiently expressed in *Nicotiana benthamiana* epidermal leaves (Fig. 1 C).

Thus, both the REM-CA and the coiled-coil domains are necessary and sufficient to target the protein to PIPmix-containing lipid bilayers. This experimental setup allowed us to further characterize the lipid-binding specificity of REM1.3.

REM1.3 mainly targets anionic lipids with exposed phosphate groups

As a first step to address the role of lipids in the binding of REM1.3, we assessed which lipids were important in this process. According to the literature (29,31,32), we formulated the hypothesis that GFP-REM1.3$_{86-198}$ (Fig. 2 A) preferentially binds to any lipid with a surface-exposed phosphate. To test this hypothesis, we generated liposomes with the same PC/ sterol mixture supplemented with different individual PIP species with one to three exposed phosphate groups at 16 mol %, i.e., PO-PI4P, PO-PI5P, di-oleoyl-PI(4,5)P_2, and palmitoyl-arachidonic-PI(3,4,5)P_3 (PA-PI(3,4,5)P_3). Fig. 2, B-E, and Table S1 showed that GFP-REM1.3$_{86-198}$ could bind to all of these anionic phospholipids.

We assessed whether PS, another abundant anionic lipid of the inner leaflet of plant PM, allowed the binding of GFP-REM1.3$_{86-198}$ to liposomes. We generated liposomes with 16 mol % POPS, but GFP-REM1.3$_{86-198}$ was not at all able to bind to those GUVs (Fig. 2 F) unless a much higher percentage of 32 mol % POPS was used (Fig. S3; Table S1). However, it was able to bind to GUVs containing 16 mol % PO-phosphatidic acid (POPA), albeit with a low binding frequency of 14% (Fig. 2 G; Table S1). Thus, the affinity of GFP-REM1.3$_{86-198}$ for PS seems much lower compared with its affinity for phospholipids with exposed phosphate groups like PIPs and PA.

As a final control, we tested GIPC, an abundant anionic sphingolipid of the plant PM's outer leaflet (45,49). Yet, GFP-REM1.3$_{86-198}$ did not bind to 1:1:1 (molar ratio) DLPC/sitosterol/GIPC GUVs (Fig. 2 H; Table S1).

PS is not necessary for REM1.3 nanodomain formation *in vivo*

We further tested the apparent superfluity of PS for REM1.3's membrane targeting *in vivo* by taking advantage of the *Arabidopsis thaliana* mutant lines of the PS synthase (*pss1-3*) completely lacking PS (21). GFP-REM1.3 was expressed in WT and *pss1* mutant background. Confocal fluorescence microscopy on *Arabidopsis thaliana* root seedlings showed GFP-REM1.3 was still targeted to the PM in the absence of PS. Furthermore, GFP-REM1.3 was partially organized in nanodomains at the PM of the *pss1-3* mutant. Thus, PS is dispensable for the addressing of REM1.3 to PM nanodomains (Fig. 3, *A-E)*. However, the nanodomains appeared larger and more diffuse in *pss1-3* than in the WT, as measured by the SCI (Fig. 3 *F*), suggesting that PS may indirectly participate in the spatial organization of REM1.3 *in vivo*.

REM1.3 is periodically organized into nanodomains on lipid vesicles

To observe individual oligomers of GFP-REM1.3$_{86-198}$ at a nanometric scale, we needed a much higher resolution than what conventional confocal microscopy can provide. We thus adapted our previously described sample preparation protocol for cryo-EM, replacing GUVs with large unilamellar vesicles and increasing the PIPmix content from 16 to 24 mol % (at the expense of DLPC), to increase the probability of spotting protein-binding events. When necessary, 0.9 µM GFP-REM1.3$_{86-198}$ was added, and the mixture was incubated at room temperature for 1 to 2 h before freezing.

Our protocol allowed us to obtain smooth, protein-free lipid vesicles (Fig. 4 *A*). In the presence of GFP- REM1.3$_{86\text{-}198,}$ we observed patterned dots decorating the vesicles' outer leaflets likely corresponding to patches of proteins, while the vesicles' inner leaflets remained smooth (Fig. 4 *B*). These protein patches shared many expected nanodomain features: 1) a finite domain size, here about 100-200 nm along the equatorial plane of the liposome; 2) a local enrichment in GFP-REM1.3$_{86\text{-}198}$ organized along the membrane with a center-to-center distance between dots of about 6.6 ± 1.1 nm; and 3) a local thickening of the outer leaflet of membrane by 4.5 ± 0.4 nm due to the presence of GFP-REM1.3$_{86\text{-}198}$ (Fig. 4 *C*).

These data demonstrate that we are indeed able to reconstitute *in vitro* membrane nanodomains of GFP- REM1.3$_{86\text{-}198}$ in lipid vesicles.

The formation of REM1.3 membrane nanodomains is protein-driven, and the shape and size of domains are phosphorylation-dependent

To gather more detailed insights into the REM1.3's nano-clustering mechanism, we used AFM on supported lipid bilayers to monitor the behavior of REM1.3 when attached to the membrane. We first generated a ''smooth'' homogeneous lipid bilayer composed of DPPC/DLPC/sitosterol/ PIPmix by heating the lipid mixture to remove preexisting lipid phase separation. In the absence of protein, no difference in height was observed on the surface of the supported lipid bilayer (Fig. 5 *A, left*). The addition of the truncated REM1.3$_{86\text{-}198}$ (purified without GFP tag; see Fig. S1) triggered the formation of thread-like domains about 8-10 nm thicker than the bulk membrane (Fig. 5 *A, middle*). To question the role of β-sitosterol, we performed AFM experiments in the absence of β-sitosterol in the saturated-unsaturated PC mixture. Fig. S4 clearly shows that the absence of β-sitosterol prevented REM1.3$_{86\text{-}198}$ from increasing the thickness of the membrane. Therefore, the presence of anionic lipids (Fig. 1) and phytosterol (Fig. S4) is not only required for the REM1.3 anchoring but also for domain formation *in vitro*.

We assessed whether preexisting lipid domain would impact the formation of REM1.3 domains. We produced heterogeneous lipid bilayers with the same lipid composition as above (see material and methods). In the absence of protein, the membrane displayed two different heights, separated just by ~1 nm, corresponding to two distinct lipid domains. Assuming that high-order lipid domains would be thicker than low-order ones (50), and considering the greater size of PIPs molecules compared with PCs, we hypothesize that the highest domains were enriched in PIPs, PS, DPPC, and sitosterol (31). After the addition of purified full-length REM1.3, we observed the formation of protein domain of ~*7* nm thick (Fig. S5) and a restructuring of the existing lipid domains. This can be interpreted as indicating that REM1.3 is interacting with and redistributing the PIPmix-enriched domains. We further used the heterogeneously expressed full-length REM1.3 (purified without GFP tag; Fig. S1) to test the potential role of the IDD in domain formation and stability. AFM observations showed that it also promoted the formation of larger, patch-like domains with a thickness around 4-10 nm (Fig. 5 B) on initially homogeneous supported lipid bilayers.

The shape and size of REM1.3 nanodomains are phosphorylation-dependent

REM1.3 can be phosphorylated by AtCPK3 *in vitro*, and the protein mobility in the membrane and nanodomain size are affected by its phosphorylation state *in vivo* (31). Thus, we tried to recreate and analyze this behavior in our minimal *in vitro* system. We phosphorylated REM1.3 *in vitro* with purified AtCPK3 from *E. coli* (Fig. S6).

The addition of phosphorylated REM1.3 to smooth membranes resulted in the creation of domains of 4-10 nm in thickness but much smaller width compared with nonphosphorylated REM1.3 (Fig. 5 C). In the case of nonphosphorylated REM1.3, the domains reached lateral dimensions of up to several hundred nanometers in width, sometimes reaching up to 1 µm, whereas the interconnected domains formed by the phosphorylated REM1.3 were not wider than 100-200 nm. This difference in phenotype *in vitro* is reminiscent of what has been observed *in vivo* by single-particle tracking photoactivated localization (29,31).

To summarize, AFM studies showed the ability of both truncated and full-length REM1.3 to trigger domain formation even in the absence of preformed lipid domains in smooth, homogeneous supported lipid bilayers. This implies that domain formation is partly protein-driven. The difference in organization pattern (thread-like for the truncated REM1.3$_{86\text{-}198}$ versus patch-like for the full-length REM1.3) implies that the IDD, which is absent in the truncated REM1.3$_{86\text{-}198}$, must indirectly play a role in supramolecular membrane nanodomain organization even though both proteins share the same membrane-binding mechanism. Phosphorylation of the REM1.3's IDD led to the disorganization of membrane domains into smaller and more disperse nanodomains.

DISCUSSION

The REM proteins are frequently involved in signaling to regulate plant biotic and abiotic interactions with their environment (18). As such, REM lateral segregation to specific nanoscale compartments at the PM are issues under high scrutiny in the fields of plant biochemistry, biophysics, and signaling.

Driving forces behind REM1.3 nanodomain formation

In this study, we assessed whether a set of three classes of lipids was sufficient to reconstitute group 1 REM nanodomains *in vitro*: 1) a mix of saturated and unsaturated bilayer-forming PCs to create lo and ld domains, 2) negatively charged polyphosphoinositides that allow the loading of REM1.3 to the bilayer (Fig. 2), and 3) phytosterols that are likely necessary to stabilize the nanodomains (Fig. S4). All of these molecules are necessary to form the protein-lipid nanodomains, located exclusively along the exposed leaflet of the bilayer, where REM1.3 is organized in a periodic manner (Fig. 4). Homomeric REM1.3 (34) targets PI4P of the PM's inner leaflet *in vivo* and other anionic lipids, albeit to a lesser extent (Fig. 2). This targeting involves the REM-CA domains through electrostatic interactions with the exposed phosphate group of PIPs and the lysine and arginine residues of REM-CA (18,29,31), while sitosterol would likely migrate to the saturated fatty acid-enriched nascent anchoring site (31). Finally, nearby REM1.3 would cluster together through their coiled-coil domains (Fig. 5 A) and more efficiently through their IDDs (Fig. 5 B), increasing nanodomain size. Indeed, disruption of the coiled-coil homomerization domain, as exemplified by GFP-REM1.3$_{EEE}$, greatly reduces, if not abolishes, membrane targeting (Fig. 1). We envision that high-order REM1.3 interactions through coiled-coil domains and IDDs likely cluster more PIPs and sitosterol. This may act as a self-amplifying system driving nanodomain formation.

Size limitation of membrane nanodomains could come from the exhaustion of nanodomain components, particularly REM1.3 and PIPs, in the immediate vicinity of the nanodomain. We assume that all nanodomain components are in equilibrium between two states: either in the bulk membrane or in membrane nanodomains. This implies that the rate of nanodomain dissociation might cancel the rate of nanodomain formation once some nanodomain size threshold is reached. To decipher such mechanisms would require a thorough kinetic analysis of nanodomain formation, which is beyond the scope of this study.

Whereas disruption of the coiled-coil homomerization domain abolishes membrane targeting, REM-CA alone still is capable of PM binding (31). This underlines the cooperative interactions of the trimerization domain toward membrane association. Our previous observation of coiled-coil domain clustering in the absence of membranes underlines the tendency of the coiled-coil domain to self-assemble (34).

Altogether, we conclude that reconstituting nanodomains of REM1.3 requires the following minimal set of partners: REM1.3$_{86\text{-}198}$, i.e., REM-CA domains bundled through a homomeric coiled-coil domain with 3 IDD (34), and PIPs, sitosterol (29,31,33), and bulk lipids, such as DPPC and DLPC, to favor the formation of two distinct lipid phases, lo and ld, respectively.

This leaves the question what drives nanodomain formation? PIPs are known to segregate from the bulk of the membrane into nanodomains without requiring any protein or sterol (24-28). Some sterols, like sitosterol, are also enriched in nanodomains in PC/PIP membranes (25). Also, lipid phase separation on supported bilayer for AFM can be achieved without REM1.3 (Fig. S5). Thus, we wished to assess whether REM1.3 had an active role in shaping membrane nanodomains or if it only targeted preexisting nanodomains. Variations in domain size and morphology, observed by AFM, upon addition of REM$_{86\text{-}198}$, REM1.3, or P-REM1.3 (Fig. 5), without or with preformed lipid domains (Fig. S5), prove REM1.3's ability to deeply modify membrane organization by forming 4-10 nm taller nanodomains. Thus, REM1.3 nanodomain formation is mostly protein-driven with the involvement of lipid to stabilize the REM domain by a feedback mechanism between proteins and lipids (see model proposed in Fig. 6 A).

Our data, delineating both an impact of the coiled-coil oligomerization as well as of the multivalent electrostatic interactions in the IDD on nanodomain clustering, could suggest the creation of a membrane-associated liquid phase separation (51). Liquid-liquid phase separation (LLPS) is a long-standing concept that gains importance through its role in multiple cellular processes (52). IDD and polymerization domains, such as coiled-coil domains, are typically overrepresented in LLPS-forming proteins (53). Shaping the features of membrane targeting and nanodomain clustering of both domains demonstrates the role of multivalent interactions that could engender phase separation on the membrane surface. The formation of a lo phase in the membrane could be orchestrated to the simultaneous creation of a separated liquid phase.

Orientation of REM1.3 at the surface of the lipid bilayer

Different models were proposed to explain the spatial organization of group1 REM: either the coiled coil is oriented perpendicular to the bilayer (18) or it lays at the surface of the membrane (1). The estimated length of the coiled coil being ~8 nm with a diameter of 2 nm (34) is compatible with the height observed with the AFM on the supported lipid bilayers but not with the cryo-EM observation of GFP-REM1.3$_{86\text{-}198}$ protruding at only 4.5 nm on the surface. This would rather suggest an orientation of REM1.3 with its coiled coil laying at the surface of the bilayer, with the REM-CAs embedded in the membrane like staples, and the IDDs interacting together. Although this hypothesis remains to be experimentally proved, it paves the ways toward elucidating the precise orientation of REM1.3 in membrane nanodomains.

Phosphorylation of REM1.3 affects nanodomain organization

The phosphorylation of REM1.3 by AtCPK3 yields a protein, P-REM1.3, that triggers a different nanodomain organization than the nonphosphorylated REM1.3 (Fig. 5 C). P-REM1.3 nanodomains have the same height but display a less compact and more disperse lateral packing on the surface of the bilayer. These data are in line with live super-resolution single-particle tracking microscopy, where we observed that the phosphorylation increases the EOS- REM1.3's diffusion coefficient and mean square displacement, reflecting an increase of REM1.3 mobility (37). Moreover, the Voronoï tessellation method comparing the *in vivo* supramolecular organization of microscopy data showed a decrease in the localization density of EOS-REM1.3 in nanodomains after phosphorylation, i.e., after infection by the potato virus X (37). Overall, the changes of REM1.3 distributions in synthetic membranes after phosphorylation phenocopy the increase of REM1.3's modulation of nanodomain organization. These data suggest the involvement of the phosphorylation of the IDD in the organization of the protein in the lipid bilayer, likely inducing conformational changes that would hinder REM1.3 oligomerization through an uncharacterized mechanism. The phosphorylated IDD could act as an entropic barrier to control nanodomain size, effectively pushing away other REM1.3 homotrimers and hindering nanodomain formation (54). Alternatively, the phosphorylation could also modulate electrostatic interactions and repulsions with other IDDs (55). Regulation by phosphorylation is also in line with our previously mentioned suggestion of LLPS formation on the membrane surface since phosphorylation is involved in LLPS modulation events (56).

Our present work of *in vitro* reconstitution paves the way to understand the labeling of different REM phylogenic groups that localize to different nanodomains and are, in some cases, completely excluded from each other (19).

SUPPORTING MATERIAL

Supporting material can be found online at https://doi.org/10.1016/j.bpj. 2022.12.035.

AUTHOR CONTRIBUTIONS

A. Legrand purified the proteins and performed the GUV experiments; D.G.-C. performed and analyzed the AFM; M.-D.J. measured the clustering of REM1.3 in pss1 and WT; M.D. and O.L. performed and analyzed cryo-EM experiments; V.B. and Y.J. produced the *pss1* line expressing fluorescent REM1.3; M.B. and A. Legrand performed the phosphorylation experiments of REM1.3; B.H., V.G., and A. Loquet advised on biophysical analyses; A. Legrand, M.V.T., and S.M. designed the project, analyzed the data, built the figures and wrote the manuscript.

ACKNOWLEDGMENTS

We thank the Bordeaux Imaging Center, part of the National Infrastructure France-BioImaging supported by the French National Research Agency (ANR-10-INBS-04). We thank Bordeaux-Metabolome platform for lipid analysis (https://www.biomemb.cnrs.fr/en/lipidomic-plateform/) supported by Bordeaux Metabolome Facility-MetaboHUB (grant no. ANR-11- INBS-0010 to S.M.). This work was supported by the French National Research Agency (grant no. ANR-19-CE13-0021 to S.M., V.G., and M.B.) and the European Research Council (ERC) under the European Union's Horizon 2020 research and innovation program (grant agreement no. 101001097 to Y.J.). The IPS2 benefits from the support of the LabEx Saclay Plant Sciences-SPS (ANR- 10-LABX-0040-SPS). We thank Dr. Frederic Daste for his help with the GUV generation protocol.

DECLARATION OF INTERESTS

The authors declare no conflict of interest.

REFERENCES

1. Jaillais, Y., and T. Ott. 2020. The nanoscale organization of the plasma membrane and its importance in signaling: a proteolipid perspective. *Plant Physiol.* 182:1682-1696.
2. Prior, I. A., P. D. Lewis, and C. Mattos. 2012. A comprehensive survey of Ras mutations in cancer. *Cancer Res*. 72:2457-2467.
3. Zhou, Y., P. Prakash,…, J. F. Hancock. 2018. Ras and the plasma membrane: a complicated relationship. *Cold Spring Harb. Perspect. Med*. 8:a031831.
4. Sartorel, E., C. Ünlü,..., D. McCusker. 2018. Phosphatidylserine and GTPase activation control Cdc42 nanoclustering to counter dissipative diffusion. *Mol. Biol. Cell*. 29:1299-1310.
5. Weise, K., S. Kapoor,..., R. Winter. 2011. Membrane-mediated induction and sorting of K-Ras microdomain signaling platforms. *J. Am. Chem. Soc.* 133:880-887.
6. Zhou, Y., P. Prakash,…, J. F. Hancock. 2017. Lipid-sorting specificity encoded in K-Ras membrane anchor regulates signal output. *Cell.* 168:239-251.e16.
7. Ewers, H., W. Römer, ..., L. Johannes. 2010. GM1 structure determines SV40-induced membrane invagination and infection. *Nat. Cell Biol.* 12:11-18.
8. Yuan, C., and L. J. Johnston. 2001. Atomic force microscopy studies of ganglioside GM1 domains in phosphatidylcholine and phosphatidylcholine/cholesterol bilayers. *Biophys. J.* 81:1059-1069.
9. Parton, R. G., and K. Simons. 2007. The multiple faces of caveolae. *Nat. Rev. Mol. Cell Biol.* 8:185-194.
10. Bramkamp, M., and D. Lopez. 2015. Exploring the existence of lipid rafts in bacteria. *Microbiol. Mol. Biol. Rev.* 79:81-100.
11. Spira, F., N. S. Mueller, ..., R. Wedlich-Söldner. 2012. Patchwork organization of the yeast plasma membrane into numerous coexisting domains. *Nat. Cell Biol*. 14:640-648.
12. Cebecauer, M., M. Amaro,..., M. Hof. 2018. Membrane lipid nanodomains. Chem. Rev. 118:11259-11297.
13. Mouritsen, O. G., and L. A. Bagatolli. 2015. Lipid domains in model membranes: a brief historical perspective. *Essays Biochem*. 57:1-19.
14. Simons, K., and W. L. C. Vaz. 2004. Model systems, lipid rafts, and cell membranes. *Annu. Rev. Biophys. Biomol. Struct.* 33:269-295.
15. Platre, M. P., V. Bayle,...., Y. Jaillais. 2019. Developmental control of plant Rho GTPase nano-organization by the lipid phosphatidylserine. *Science.* 364:57-62.
16. Smokvarska, M., C. Francis,..., A. Martiniere. 2020. A plasma membrane nanoplatform ensures signal specificity during osmotic signaling in plants. *Curr. Biol.* 30:4654-4664.e4.
17. Raffaele, S., S. Mongrand,..., T. Ott. 2007. Genome-wide annotation of remorins, a plant-specific protein family: evolutionary and functional perspectives. *Plant Physiol.* 145:593-600.
18. Gouguet, P., J. Gronnier,..., V. Germain. 2021. Connecting the dots: from nanodomains to physiological functions of REMORINs. *Plant Physiol.* 185:632-649.
19. Jarsch, I. K., S. S. A. Konrad,..., T. Ott. 2014. Plasma membranes are subcompartmentalized into a plethora of coexisting and diverse microdomains in Arabidopsis and Nicotiana benthamiana. *Plant Cell.* 26:1698-1711.
20. Barbosa, I. C. R., H. Shikata,..., C. Schwechheimer. 2016. Phospho-lipid composition and a polybasic motif determine D6 protein kinase polar association with the plasma membrane and tropic responses. *Development (Cambridge, U. K.)*. 143:4687-4700.
21. Platre, M. P., L. C. Noack,..., Y. Jaillais. 2018. A combinatorial lipid code shapes the electrostatic landscape of plant endomembranes. *Dev. Cell.* 45:465-480.e11.
22. Simon, M. L. A., M. P. Platre,..., Y. Jaillais. 2016. A PtdIns(4)P-driven electrostatic field controls cell membrane identity and signalling in plants. *Nature Plants.* 2:16089.
23. Synek, L., R. Pleskot,..., M. Potocky. 2021. Plasma membrane phospholipid signature recruits the plant exocyst complex via the EXO70A1 subunit. *Proc. Natl. Acad. Sci. USA*. 118:e2105287118.
24. Bilkova, E., R. Pleskot, ..., U. Coskun. 2017. Calcium directly regulates phosphatidylinositol 4, 5-bisphosphate headgroup

conformation and recognition. *J. Am. Chem. Soc.* 139:4019-4024.

25. Furt, F., S. Konig, ..., S. Mongrand. 2010. Phosphoinositides are enriched in plant membrane rafts and form microdomains in the plasma membrane. *Plant Physiol.* 152:2173-2187.
26. Ji, C., Y. Zhang,..., X. Lou. 2015. Nanoscale landscape of phosphoinositides revealed by specific pleckstrin homology (PH) domains using single-molecule super resolution imaging in the plasma membrane. *J. Biol. Chem*. 290:26978-26993.
27. Motegi, T., K. Takiguchi,..., R. Tero. 2021. Physical properties and reactivity of microdomains in phosphatidylinositol-containing supported lipid bilayer. *Membranes.* 11:339.
28. van den Bogaart, G., K. Meyenberg,..., R. Jahn. 2011. Membrane protein sequestering by ionic protein-lipid interactions. *Nature*. 479:552-555.
29. Gronnier, J., J.-M. Crowet,..., S. Mongrand. 2017. Structural basis for plant plasma membrane protein dynamics and organization into functional nanodomains. *Elife*. 6:e26404.
30. Konrad, S. S. A., C. Popp,..., T. Ott. 2014. S-acylation anchors remorin proteins to the plasma membrane but does not primarily determine their localization in membrane microdomains. *New Phytol*. 203:758-769.
31. Legrand, A., D. Martinez,..., B. Habenstein. 2019. Nanodomain clustering of the plant protein remorin by solid-state NMR. *Front. Mol. Biosci*. 6:107.
32. Perraki, A., J.-L. Cacas,..., S. Raffaele. 2012. Plasma membrane localization of Solanum tuberosum remorin from group 1, homolog 3 is mediated by conformational changes in a novel C-terminal anchor and required for the restriction of potato virus X movement. *Plant Physiol.* 160:624-637.
33. Raffaele, S., E. Bayer,..., S. Mongrand. 2009. Remorin, a solanaceae protein resident in membrane rafts and plasmodesmata, impairs potato virus X movement. *Plant Cell.* 21:1541-1555.
34. Martinez, D., A. Legrand,..., B. Habenstein. 2019. Coiled-coil oligomerization controls localization of the plasma membrane REMORINs. *J. Struct. Biol.* 206:12-19.
35. Marin, M., V. Thallmair, and T. Ott. 2012. The intrinsically disordered N-terminal region of AtREM1.3 remorin protein mediates protein-protein interactions. *J. Biol. Chem.* 287:39982-39991.
36. Marin, M., and T. Ott. 2012. Phosphorylation of intrinsically disordered regions in remorin proteins. *Front. Plant Sci.* 3:86.
37. Perraki, A., J. Gronnier,..., V. Germain. 2018. REM1.3's phospho-status defines its plasma membrane nanodomain organization and activity in restricting PVX cell-to-cell movement. *PLoS Pathog.* 14:e1007378.
38. Bah, A., R. M. Vernon,..., J. D. Forman-Kay. 2015. Folding of an intrinsically disordered protein by phosphorylation as a regulatory switch. *Nature.* 519:106-109.
39. Uversky, V. N. 2013. A decade and a half of protein intrinsic disorder: biology still waits for physics. *Protein Sci.* 22:693-724.
40. Mamode Cassim, A., Y. Navon,..., S. Mongrand. 2021. Biophysical analysis of the plant-specific GIPC sphingolipids reveals multiple modes of membrane regulation. *J. Biol. Chem.* 296:100602.
41. Zacharias, D. A., J. D. Violin,..., R. Y. Tsien. 2002. Partitioning of lipid-modified monomeric GFPs into membrane microdomains of live cells. *Science.* 296:913-916.
42. Boudsocq, M., M.-J. Droillard,..., C. Lauriere. 2012. Characterization of Arabidopsis calcium-dependent protein kinases: activated or not by calcium? *Biochem. J.* 447:291-299.
43. McGuffin, L. J., K. Bryson, and D. T. Jones. 2000. The PSIPRED protein structure prediction server. *Bioinformatics.* 16:404-405.
44. Mirdita, M., K. Sch€utze,..., M. Steinegger. 2022. ColabFold: making protein folding accessible to all. *Nat. Methods.* 19:679-682.
45. Cacas, J.-L., C. Bure, ..., S. Mongrand. 2016. Revisiting plant plasma membrane lipids in tobacco: a focus on sphingolipids. *Plant Physiol.* 170:367-384.
46. Feigenson, G. W., and J. T. Buboltz. 2001. Ternary phase diagram of dipalmitoyl-PC/dilauroyl-PC/cholesterol: nanoscopic domain formation driven by cholesterol. *Biophys. J.* 80:2775-2788.
47. Ingolfsson, H. I., M. N. Melo,..., S. J. Marrink. 2014. Lipid organization of the plasma membrane. *J. Am. Chem. Soc.* 136:14554-14559.
48. Salvemini, I. L., D. M. Gau,..., P. D. J. Moens. 2014. Low PIP(2) molar fractions induce nanometer size clustering in giant unilamellar vesicles. *Chem. Phys. Lipids.* 177:51-63.
49. Cassim, A. M., Y. Navon,..., S. Mongrand. 2020. Purification, characterization and influence on membrane properties of the plant-specific sphingolipids GIPC. Preprint at bioRxiv. https://doi.org/10.1101/ 2020.10.01.313304.

50. Grelard, A., P. Guichard,..., E. J. Dufourc. 2013. Hepatitis B subvirus particles display both a fluid bilayer membrane and a strong resistance to freeze drying: a study by solid-state NMR, light scattering, and cryo-electron microscopy/tomography. *Faseb. J.* 27:4316-4326.

51. Ditlev, J. A. 2021. Membrane-associated phase separation: organization and function emerge from a two-dimensional milieu. *J. Mol. Cell Biol.* 13:319-324.

52. Li, P., S. Banjade,..., M. K. Rosen. 2012. Phase transitions in the assembly of multivalent signalling proteins. *Nature.* 483:336-340.

53. Alberti, S., A. Gladfelter, and T. Mittag. 2019. Considerations and challenges in studying liquid-liquid phase separation and biomolecular condensates. *Cell.* 176:419-434.

54. Jamecna, D., J. Polidori,..., B. Antonny. 2019. An intrinsically disordered region in OSBP acts as an entropic barrier to control protein dynamics and orientation at membrane contact sites. *Dev. Cell.* 49:220- 234.e8.

55. Liu, B., D. Chia,..., C. C. Gradinaru. 2014. The effect of intrachain electrostatic repulsion on conformational disorder and dynamics of the Sic1 protein. *J. Phys. Chem. B.* 118:4088-4097.

56. Wang, B., L. Zhang,..., F. Zhou. 2021. Liquid-liquid phase separation in human health and diseases. *Signal Transduct. Targeted Ther.* 6:290-316.

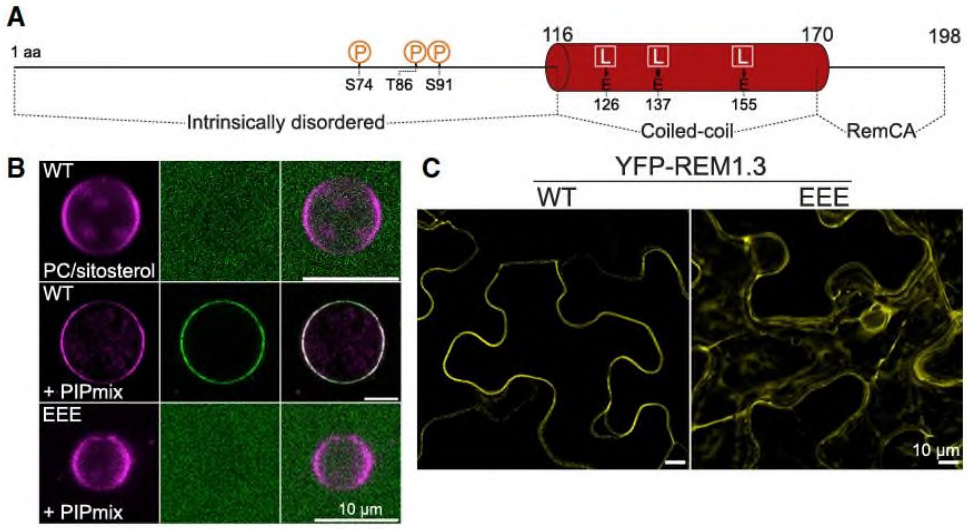

Figure 1. Minimal setting to address REM1.3's organization in artificial membranes. Disrupting of REM1.3's coiled-coil domain hampers membrane targeting. (A) Stick figure representing the different domains of StREM1.3. Red cylinder: coiled-coil domain with critical hydrophobic residues (white) and point mutations (black) used in this study. P represents phosphorylation sites. REM-CA, remorin C-terminal anchor. (B) Membrane targeting of GFP-REM1.3$_{86\text{-}198}$ in GUVs composed of DPPC/ DLPC/sitosterol, 8/50/42 mol % (top), or against DPPC/DLPC/sitosterol/PIPmix, 50/26/8/16 mol % (middle), or GFP-REM1.3$_{86\text{-}198EEE}$ against GUVs of DPPC/DLPC/sitosterol/PIPmix 50/26/8/16 mol % (bottom) (molar percentages). Left: RhodPE channel (magenta). Middle: GFP-REM1.3$_{86\text{-}198}$ channel (green). Right: composite images from both channels. Observation statistics are given in Table S1. (C) Membrane targeting of GFP- REM1.3 WT or EEE transiently expressed in *N. benthamiana* leaves. Scale bars: 10 µm.

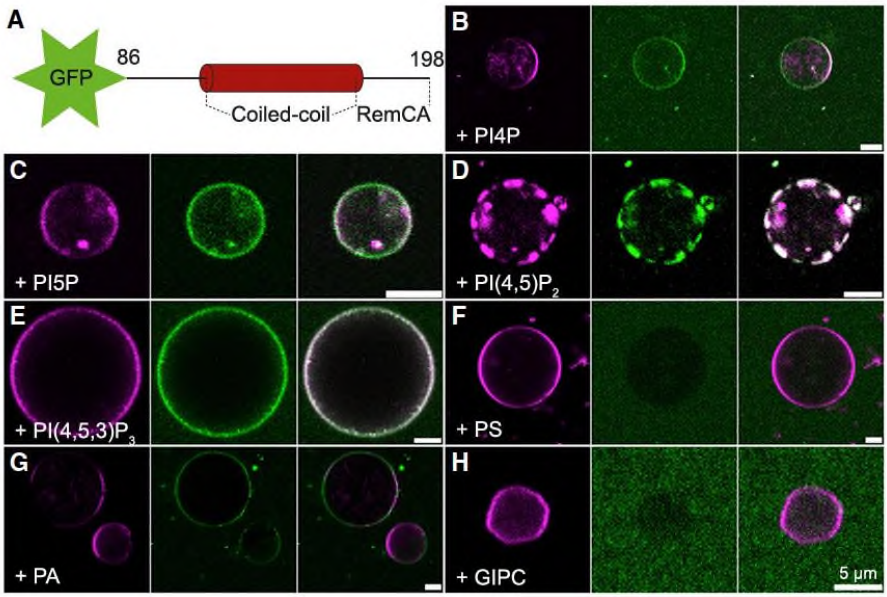

Figure 2. REM1.3 binds to GUVs containing PIPs or PA but neither PS nor GIPCs. (A) Stick figure of the purified protein GFP-REM1.3$_{86\text{-}198}$ used. GUVs containing DPPC/DLPC/sitosterol 50/26/8 mol % supplemented with 16 mol % POPI4P (B) ; POPI5P (C) ; DOPI(4,5)P_2 (D) ; PAPI(3,4,5)P_3 (E) ; POPS (F) ; POPA (G) ; or GIPC (H) were mixed with ~$1.8.10^{-12}$ mol GFP-REM1.3$_{86\text{-}198}$. Left: RhodPE channel (magenta). Middle: GFP-REM1.3$_{86\text{-}198}$ channel (green). Right: composite images from both channels. Scale bars: 5 µm. Observation statistics are given in Table S1.

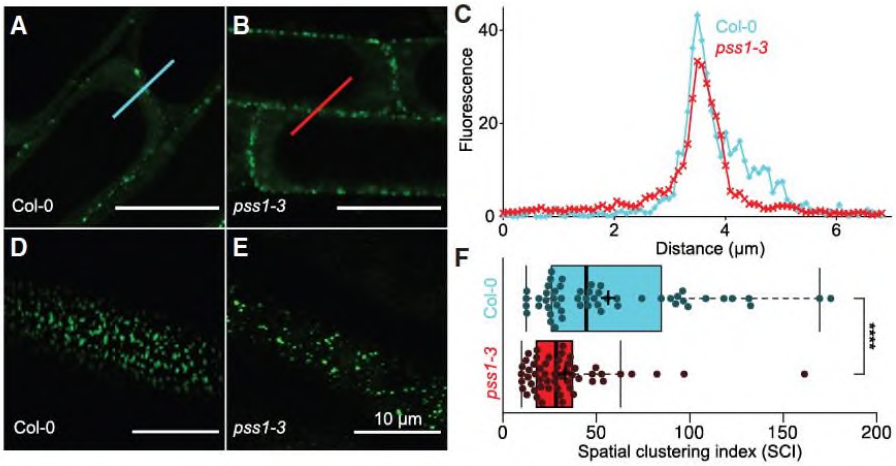

Figure 3. PS defines nanoclustering pattern but not membrane targeting of REM1.3 *in vivo*. (A and B) Cross-section confocal images of epidermal cells of Col-0 (A) or *pss1-3* KO (B) *Arabidopsis thaliana* 6-day-old root seedlings. (C) Fluorescence profiles for traces in (A, cyan) and (B, red) are drawn. (D and E) Surface-view confocal images of epidermal cells of Col-0 (D) or *pss1-3* KO (E) *Arabidopsis thaliana* 6-day-old root seedlings. (F) Spatial clustering index was calculated using surface-view confocal images (D and E). Tukey boxplots show the mean fluorescence intensity and the spatial clustering index of YFP-REM1.3 of at least 18 cells from three independent experiments. Significance was determined using a Student's t-test (****$p < 0.001$). Scale bars: 10 µm.

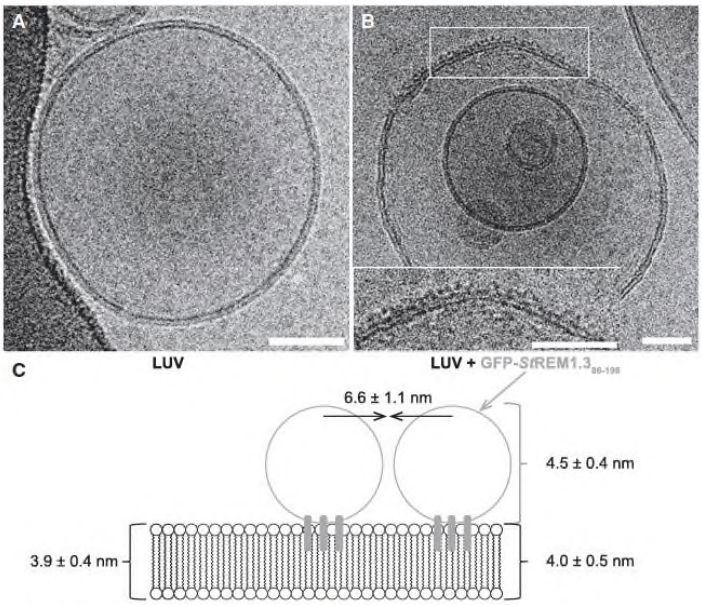

Figure 4. Cryo-EM reveals nanodomain segregation of GFP-REM1.3$_{86-198}$ in large unilamellar vesicles (LUVs) containing PIPmix. (*A*) A protein-free LUV composed of DPPC/DLPC/sitosterol/PIPmix (50/18/8/24 mol %). (*B*) GFP-REM1.3$_{86-198}$ bound to a LUV. Notice the uneven distribution of protein and total thickness along its equatorial plane. Insert: zoom onto a GFP-REM1.3$_{86-198}$-rich membrane domain. (*C*) Schematic representation of three GFP-REM1.3$_{86-198}$ bound to a membrane: the three gray lines represent REM-CA, and the balls represent the 3 REM-IDD-coiled coil fused to GFP. Measured thicknesses for membrane and membranes under REM1.3 and REM1.3-REM1.3 are provided (n = 20). Scale bars: 50 nm.

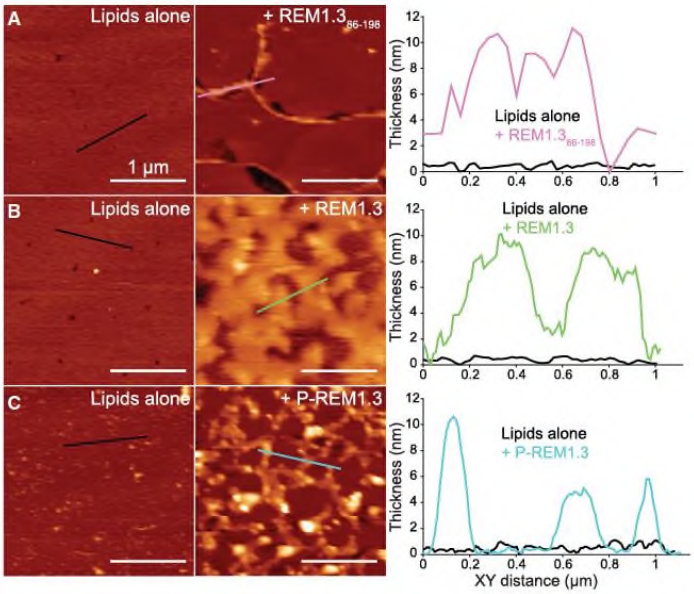

Figure 5. REM1.3-driven nanodomain formation by AFM. Small unilamellar vesicles made of DPPC/DLPC/sitosterol/ PIPmix (50/18/8/24 mol %) are deposited on a mica plate. (A) A smooth membrane (left) generated by incubating the lipid mixture overnight at 30ºC was incubated for 30 min with REM1.3$_{86\text{-}198}$ (middle). The profiles under the two lines in the images are indicated in the right panel. (B and C) Similarly, a smooth membrane (left) was incubated for 30 min with full-length REM1.3 (middle) either nonphosphorylated (B) or phosphorylated by AtCPK3 (C). The profiles under the two lines in the images are indicated in the right panel. Images shown are representative of those found in at least three independent experiments. Scale bars: 1 µm.

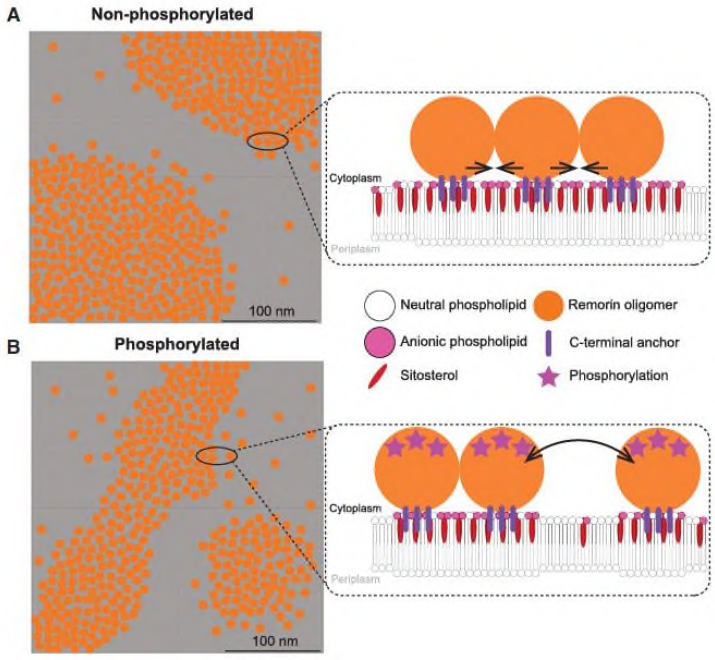

Figure 6. Schematic of the phosphodependent REM1.3 membrane nanodomain formation. REM1.3 oligomers bind to anionic phospholipids (PIPs and PA but not PS) of the PM's inner leaflet and cluster into membrane nanodomains in the presence of sitosterol. Membrane nanodomain size depends on REM1.3's phosphorylation state: (A) a few hundreds of nanometers if REM1.3 is not phosphorylated but (B) only about 100 nm if REM1.3 is phosphorylated. Insert: a close-up lateral view of this process depicts REM1.3 clustering with anionic phospholipids (PIPS and PA but not PS) and sitosterol, resulting in a slight increase in lipid order (31). Protein-protein interactions (black arrows) and phosphorylations define the size and the microscopic organization pattern of REM1.3 membrane nanodomains.

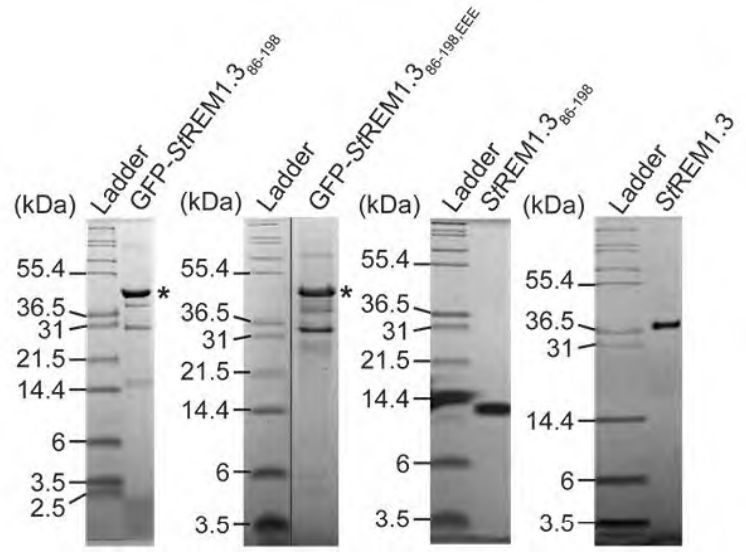

Figure S1. Purity of proteins used in this study. GFP-REM1.3$_{86\text{-}198}$, GFP-REM1.3$_{86\text{-}198,\ EEE}$, REM1.3$_{86\text{-}198}$, and REM1.3 were loaded on a tris-tricine 13% (w/v) polyacrylamide gel. Protein standard (ladder) was Mark 12 protein standard from ThermoFisher. Stars indicate GFP-REM1.3$_{86\text{-}198}$ and GFP- REM1.3$_{86\text{-}198,EEE}$, respectively.

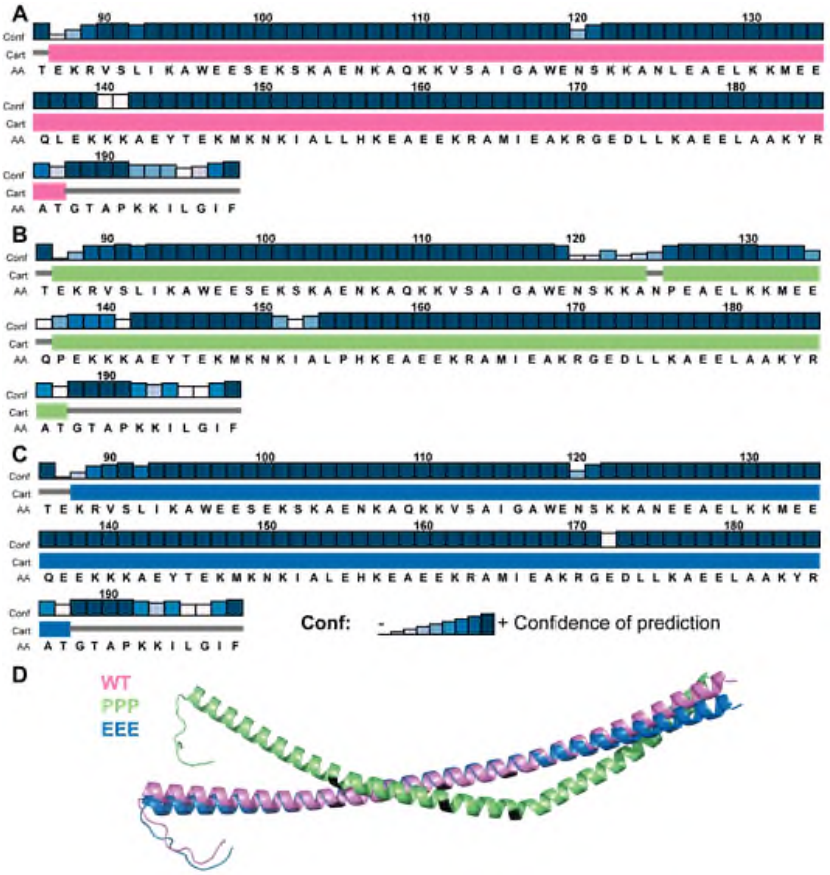

Figure S2. Structure predictions for REM$_{86\text{-}198}$, WT, REM$_{86\text{-}198,\ PPP}$, and REM$_{86\text{-}198,\ EEE}$. PsiPred structure predictions for REM$_{86\text{-}198}$, WT (A, pink), REM$_{86\text{-}198,\ PPP}$ (B, green), and REM$_{86\text{-}198,\ EEE}$ (C, blue), and AlphaFold-generated structural models thereof (D). Residues 126, 137, and 155 are labelled in black. Conf: confidence of prediction (scale from 0 to 8). Cart: cartoon representation of helices, either coil (gray thin bars) or helix (colourful large bars).

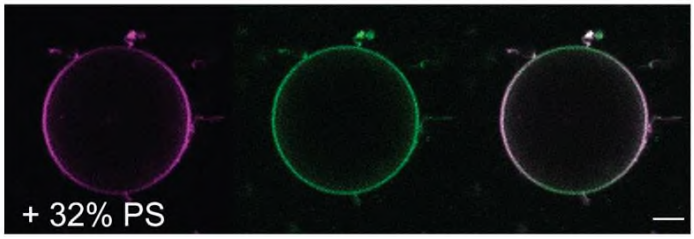

Figure S3. GFP-REM1.3$_{86\text{-}198}$ binds to GUVs enriched with 32 mol% POPS. A GUV containing DPPC/DLPC/sitosterol/ POPS 40/21/6/32 mol% is incubated with GFP-REM1.3$_{86\text{-}198}$. *Left*: RhodPE channel (magenta). *Middle*: GFP-REM1.3$_{86\text{-}198}$ channel (green). *Right*: composite image from both channels. Scale bar: 5 µm. Observation statistics are given in Table S1.

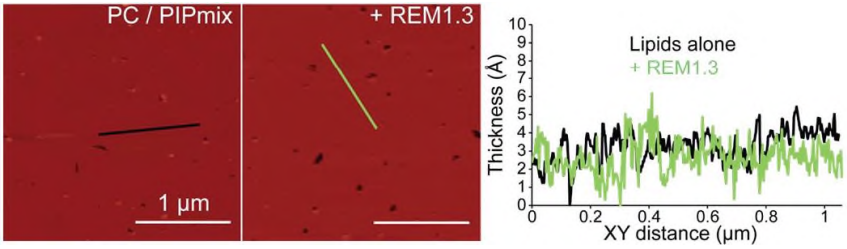

Figure S4. PIPs and β-sitosterol are required for nanodomain formation. A bilayer composed of DPPC/DLPC/PIPmix (50/18/24 mol%) (left) is incubated with 2 µM of REM1.3$_{86\text{-}198}$ for 30 min (middle). Thickness profiles of lines drawn on both images are provided (right).

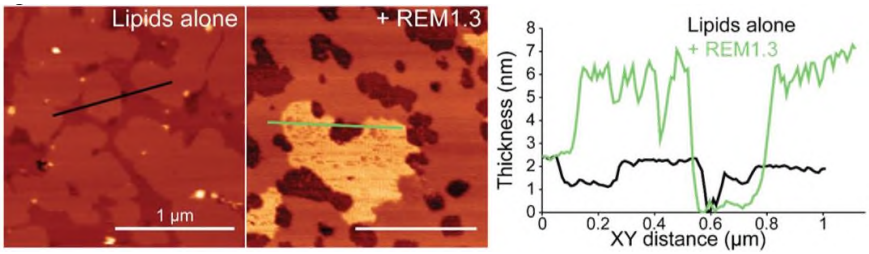

Figure S5. Full-length REM1.3 forms nanodomains in a supported bilayer with pre-existing lipid domains. AFM observation of a patchy membrane with pre-existing lipid domain (generated without heating the lipid mixture) was incubated for 30 min with full-length REM1.3. Two thickness representative profiles are provided (right). Experiments were performed 4 times with different mica substrates, and representative are presented in the Figure. Scale bars: 1 µm.

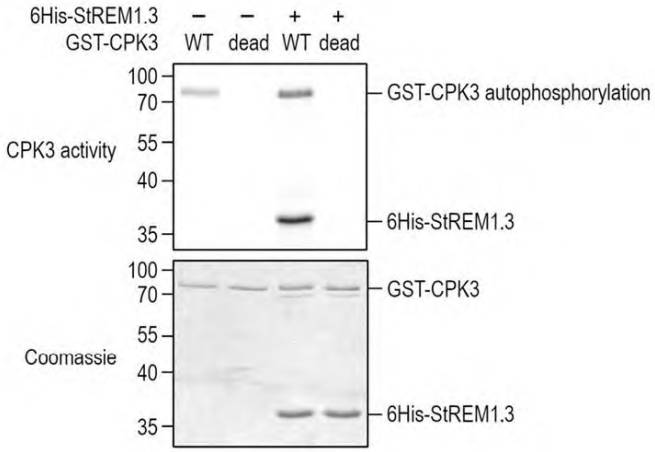

Figure S6. *In vitro* phosphorylation assay of REM1.3 by AtCPK3. 6His-REM1.3 and GST-AtCPK3 (WT and dead D202A) were purified from *E. coli* and mixed to a ratio of 4:1 for *in vitro* kinase assay. Bands corresponding to autophosphorylation of GST-AtCPK3 and transphosphorylation of 6His-REM1.3 are indicated (top). Gel was stained by coomassie blue to visualize protein loading (bottom).

Condition	Observed liposomes	Binding events	Binding frequency
ϕ	17	0	0
PIPmix	374	287	0.767379679
PIPmix (EEE)	205	12	0.058536585
POPI4P	187	103	0.550802139
POPI5P	1156	385	0.333044983
DOPI(4,5)P_2	327	208	0.636085627
PAPI(3,4,5)P_3	17	16	0.941176471
16% POPS	272	0	0
32% POPS	311	195	0.627009646
POPA	974	134	0.137577002
GIPC	5	0	0

Table S1. Statistics for GUV observations by confocal microscopy. Number of observed GUVs (observed liposomes) and number of GUVs showing GFP-REM1.3$_{86-198}$ binding (binding events). Binding frequency: ratio of the number of binding events over the number of observed liposomes. Φ : DPPC /DLP /sitosterol 50/42/8 mol % GUVs in presence of GFP-REM1.3$_{86-198}$. PIPmix (EEE): DPPC/DLPC/sitosterol/PIPmix 50/26/8/16 mol% GUVs in presence of GFP-REM1.3$_{86-198,EEE}$ (Figure 1B). High PS: DPPC/DLPC/sitosterol/POPS 40/21/6/32 mol% GUVs in presence of GFP-REM1.3$_{86-198}$ (see Figure S2).